

# Biomechanical characterization of scallop shells exposed to ocean acidification and warming

Aldo F. Abarca-Ortega<sup>a,e</sup>, Estefano Muñoz-Moya<sup>a</sup>, Matías Pacheco A.<sup>a</sup>, Claudio M. García-Herrera<sup>a</sup>, Diego J. Celentano<sup>b</sup>, Nelson A. Lagos<sup>c</sup>, Marco A. Lardies<sup>d</sup>

<sup>a</sup>Departamento de Ingeniería Mecánica, Universidad de Santiago de Chile, Av. Bernardo O'Higgins 3363, Santiago de Chile, Chile

<sup>b</sup>Departamento de Ingeniería Mecánica y Metalúrgica, Pontificia Universidad Católica de Chile, Av. Vicuña Mackenna 4860, Santiago de Chile, Chile

<sup>c</sup>Centro de Investigación e Innovación para el cambio climático (CiiCC), Universidad Santo Tomás, Av. Ejército Libertador 146, Santiago de Chile, Chile

<sup>d</sup>Departamento de Ciencias, Facultad de Artes Liberales, Universidad Adolfo Ibáñez, Santiago, Chile

<sup>e</sup>Center for Biomedical Technology, Universidad Politécnica de Madrid, 28223 Pozuelo de Alarcón, Spain

---

## Abstract

Increased levels of Carbon dioxide ( $\text{CO}_2$ ) in the atmosphere triggered a cascade of physical and chemical changes in the ocean surface. Marine organism producing shell carbonates are regarded as vulnerable to these physical (warming) and chemical (acidification) changes occurring in the oceans. In the last decade, the aquaculture production of the bivalve scallop *Argopecten purpuratus* (*AP*) showed declined trends along the Chilean coast. These negative trends have been ascribed to ecophysiological and biomineralization constraints in shell carbonates production. This work experimentally characterizes the biomechanical response of *AP* scallop shells subjected to climate change scenarios (acidification and warming) via quasi-static tensile and flexocompression tests. The experimental results indicate the adaptation of mechanical properties to hostile growth scenarios in terms of temperature and water acidification. In addition, the mechanical response of the *AP* subjected to control climate conditions was analyzed with finite element simulations including an anisotropic elastic constitutive model for a two-fold purpose: firstly, to calibrate the material model parameters using the tensile test curves in two mutually perpendicular directions (representative of the mechanical behavior of the material) and, secondly, to validate this characterization procedure in the prediction of the macromechanical behavior of the material in two mechanical tests (tensile test in a third direction of  $45^\circ$  with respect to the two previous ones and the flexocompression test on the whole shell).

## Author Summary

*AP* aquaculture activities present a negative trend during the last decades, and only 20% of the production levels observed at 2004 have been harvested during 2014. This drastic reduction in the production of cultured scallops impact on the socioeconomic sustainability of this industrial sector in northern Chile, thus making necessary to understand the

causes of this reduction in production in order to find ways to adapt to it. One of the most important processes of scallop aquaculture procedures is thinning, a sorting in which individuals are separated by size using mechanical sifting. To overcome this process, the individual shells must be strong enough to avoid fracture and thus, reduce the loss of the scallops production. The impact of projected ocean acidification and warming as result of the increased anthropogenic CO<sub>2</sub> levels in the atmosphere have been postulated as the major threat for marine calcifiers. In particular, mollusks are recognized as one of the most vulnerable groups to ocean acidification, particularly affecting carbonate precipitation or dissolution, and their growth rates and shell strength and functionality. In the present study we evaluate for the first time the biomechanical elastic properties on tension and flexocompression of *AP* exposed experimentally to ocean acidification and warming condition. Our results will provide critical information about the vulnerability of the resources to ongoing ocean changes and to establish adaptation strategies aimed to improve the sustainability of the socioeconomic sector and local communities.

*Keywords:* Bivalves, Ocean acidification, Numerical simulation, Finite element analysis, Elastic anisotropy

---

## **1. Introduction**

It is known that about one third of the CO<sub>2</sub> emissions produced by human activities are deposited on the ocean surface [1]. In addition to global warming effects, the CO<sub>2</sub> sinks through the ocean surface, altering the pH of the seawater and its carbon concentration, a process known as Ocean Acidification (OA) to describe the reduction of the pH level of seawater [2]. By the end of this century, seawater is expected to become more acidic, changing its pH from ca. 8.0 to 7.8, and reaching pH 7.6 by the year 2200 [3]. Recent studies indicate that the Chilean coastal upwelling areas (30° South latitude) have naturally low pH (acidic) and high concentrations of dissolved carbon dioxide [4], conditions that are exposed to a progressive acidification described for other coasts such as Oregon and California upwelling ecosystems [5, 6]. In these regions, the major impacts of ocean acidification was evidenced in a significant reduction in production of the cultured oyster *Crassostrea gigas* [7]. Due to these evidence and the similarity with the upwelling conditions operating along the Chilean coast, it can be suggested that these environmental impacts can also be affecting the production and sustainability of the scallop aquaculture industry in northern Chile, which have also shown a decreasing trend in landings over the last two decades [8, 9]. In a recent study, Ramajo et al. [10] suggest that *Argopecten purpuratus* (*AP*) in its juvenile stage prioritizes calcification at the expense of growth under acidic conditions, being a factor not so sensitive compared to the temperature of its habitat which is associated with early or late mortalities, observing significantly higher mortality at 18°C than at 14°C.

21

---

*Email address:* claudio.garcia@usach.cl (Claudio M. García-Herrera )

22 The shell of mollusks is a material composed of two parts, i.e., a first organic protein part  
23 (5-10%) that covers a second part composed by calcium carbonate crystals ( $\text{CaCO}_3$ ) in a  
24 calcite or aragonite state, constituting over 90-95% of the total material [11, 12]. In the case  
25 of bivalves, in particular, the microstructure of the scallop shell crystallography may have  
26 various configurations or combinations. These configurations can be categorized into eight  
27 types, namely: simple prismatic, composite prismatic, nacreous cells, nacreous lenticular,  
28 foliated, crossed-lamellar, complex crossed-lamellar, and homogeneous structures, which are  
29 species specific, requiring particular studies to understand the role of these crystallographies  
30 on the shell properties expressed at the nano, micro or macro scales [13–15]. In the case  
31 of the *Pectinidae* family of mollusks, to which *AP* belongs, they present leaflets composed  
32 almost entirely by calcite crystals, characterized by having an internal layer with foliated  
33 and prismatic microstructure, a middle layer with a foliated microstructure, and an external  
34 layer with crossed laminar microstructure [14]. The analysis of these materials, considering  
35 the microstructure, is still a very complex challenge. As a first estimate, a feasible approach  
36 is to consider the material as a composite solid in the context of continuum mechanics.  
37

38 The characterization of shells under uniaxial tensile stress has only been reported on  
39 the research in Indonesian white pearl oysters by Chen et al. [16], where the grips and  
40 samples were designed for this purpose, in addition to analyzing the fracture of the material  
41 using acoustic emission measurements. There are very few systematic studies aimed at  
42 understanding the impacts of the climate stressors like OA and warming upon the biome-  
43 chanical properties of the mollusk shells. For instance, Meng et al. [17] studied the effect  
44 of acidity (increased  $\text{CO}_2$  concentration) on oysters (*Magallana hongkongensis*), concluding  
45 a readjustment in the structural integrity, crystallographic orientation, and mechanical  
46 characteristics of the shell, constituting a decrease in the stiffness of the material in terms  
47 of micro-scale properties. Other studies show negative effects of environmental acidity on  
48 the structure and molecular composition of marine animals, which affects their mechanical  
49 response. Dery et al. [18] describes how coralline algae (*Lithothamnion glaciale*) are affected  
50 in their absorption of nutrients in acidic environments, increasing their structural stiffness.  
51 Similarly, Ragazzola et al. [19] also describe an increase in the stiffness of the material  
52 of echinoderms (*Eucidaris tribuloides*) when subjected to acid or corrosive environments,  
53 postulating a response to predation, but it affects the energy allocation of the animal in its  
54 growth. Abarca [20] carried out studies on juvenile *AP* (same samples used for the present  
55 study) measuring organic content and composition, crystallography and biomechanical  
56 properties (to compression), results that indicate significant changes in the composition of  
57 the external part of the shell, which validates what Ramajo et al. [10] study. Other authors  
58 showed that acidification increases the orientation disorder of calcite crystals and reduces  
59 their mineral density around 20% (Lagos et al. submitted). However, in the groups studied,  
60 the only significant differences found in mechanical properties at compression were between  
61 test directions, i.e., orthotropic anisotropy was found precluding, therefore, the possibility  
62 of bimodularity or extending the study to other types of tests.

63 It is well established that mechanical testing and the characterization of materials is of  
64

65 primary significance for the prediction of more complex structures made up of them. This  
66 task is generally done using computational analysis tools as it is the case with the finite  
67 element method (FEM). The experimental procedure generally used for the characterization  
68 of materials is based on standards in its design, use and measurement. However, in cases  
69 where specimens have a very complex and specific geometry, validation of the applied meth-  
70 ods is required when it is not possible to perform them on a regular basis, which implies  
71 a computational numerical analysis of the method. A powerful and highly accurate tool  
72 for the digitization of real geometries, among other analyses, is the use of computational  
73 microtomography (micro-CT) scanners, where 3D reconstruction volumes can be obtained  
74 layer by layer, in order to mesh the geometry and carry out a numerical simulation using  
75 FEM. This technology allows to perform an inverse adjustment of the mechanical properties  
76 in these complex geometries, and thus to compare the real mechanical response of the  
77 experimental tests with the corresponding numerical simulation.

78  
79 The aim of this work is the experimental characterization of the anisotropic biomechani-  
80 cal behavior of *AP* shells at the macro level, which have been subjected to different climate  
81 change scenarios in its juvenile stage, and thus evaluate if the environmental physicochemical  
82 variables, expected in the future due to the influence of climate change, affect the mechanical  
83 properties of the shells in the most critical growth stage of the species. Considering these  
84 factors, two experimental tests have been designed and proposed - tensile test in two orthog-  
85 onal directions representative of the material behavior: longitudinal ( $90^\circ$ ) and transversal  
86 ( $0^\circ$ ), and a tensile test in the diagonal direction ( $45^\circ$ ); and the flexocompression test on  
87 the complete shell, based on the existing bibliography - implementing an orthotropic linear  
88 elastic model for the brittle shell material. The second objective of this research is, once  
89 the experimental tests have been performed and considering the complex and non-standard  
90 geometries used, to perform an adjustment in the macro-level biomechanical properties ob-  
91 tained from the experimental tests. The adjustment is performed by numerical simulations  
92 using FEM and, through an iterative process, adjust the mechanical properties, first in the  
93 longitudinal direction ( $90^\circ$ ), and then the transversal direction ( $0^\circ$ ). Finally, the results are  
94 validated with numerical simulations of the two proposed tests, the tensile test on the spec-  
95 imen corresponding to the diagonal direction ( $45^\circ$ ) and the flexocompression test - using the  
96 mechanical properties of the thickness direction from the literature - on the full shell. Using  
97 micro-CT technology, the three specimens and the complete shell are digitized.

98 **2. Materials and methods**

99 *2.1. Experimental procedure*

100 *2.1.1. Material*

101 Shells of chilean scallops *AP*, in its juvenile stage (<4 cm shell length) with their diluted  
102 organic joints were used due to the time they have been dead (about one year at the time  
103 of the initial biological researches in 2017 of Lagos et al. [8], Lardies et al. [9]) were exposed  
104 to the combination of ocean acidification (pH 7.6 – 8.1) and warming (temperature 14 °C –  
105 18 °C). The control conditions are represented by the combination of 14 °C and pH 8.1 for

106 current temperature and acidification conditions measured observed in Tongoy Bay ( $30^{\circ} 12'$   
107 S,  $71^{\circ} 34' O$ ), were the scallop aquaculture activities are performed. A detailed description  
108 of the experimental setting and impact on ecophysiology and shell morphology at the macro  
109 scale are described in Lagos et al. [8] and Lardies et al. [9].  
110

111 The four experimental treatments combining temperature and acidification scenarios  
112 were: (1)  $14^{\circ}C$  and pH  $\sim 8.1$  present-day averaged conditions observed in Tongoy bay were  
113 scallops are cultivated (i.e., control); (2)  $14^{\circ}C$  and low pH  $\sim 7.6$  resembling acidification  
114 condition at control temperature; (3)  $18^{\circ}C$  and control pH  $\sim 8.1$  representing warming  
115 conditions; and (4)  $18^{\circ}C$  and pH  $\sim 7.6$  representing the combined effect of warming and  
116 acidification. Control temperature represent averaged conditions recorded during the scallop  
117 collection, whereas high temperature treatment, in addition to the projected increase in  $4$   
118  $^{\circ}C$  (IPCC 2014), represents the maximum surface temperature ( $18^{\circ}C$ ) reported for Tongoy  
119 Bay in summer season [8]. In each scenario, the temperature was stabilized using chillers  
120 ( $\pm 0.1^{\circ}C$ ), while the pH scenarios was achieved by bubbling only atmospheric air was into  
121 experimental aquaria for present-day control conditions (i.e.,  $< 400 \mu\text{atm } \rho\text{CO}_2$  in seawater  
122 for 2015) and bubbling a compressed (117 psi) mix of air plus pure CO<sub>2</sub> and bubbled into  
123 aquaria using mass flow controllers (MFCs, AalborgTM), reaching  $\sim 900 \mu\text{atm } \rho\text{CO}_2$  in  
124 seawater, which resulted in a drop of pH  $\sim 0.3$  units, yielding a target pH level of  $\sim 7.6$  for  
125 the acidification scenario, while the present-day pH level remained at pH  $\sim 8.0$  units. These  
126  $\rho\text{CO}_2$  levels in seawater take account of the rate of change projected for the atmospheric CO<sub>2</sub>  
127 by the year 2100, which is in agreement with IPCC A2 emission scenario (e.g. Meinshausen  
128 et al. [21]). The seawater of each aquaria was replaced every 2 days using the pre-equilibrated  
129 seawater. The resulting mean ( $\pm \text{SE}$ ) conditions in temperature, pH and  $\rho\text{CO}_2$  in seawater  
130 for each treatment are described in Lagos et al. [8] and Lardies et al. [9]. The experimental  
131 exposure lasted 20 days. After the experimental period the animals were euthanized to make  
132 measurements of the shells and tissue weight [8, 9], and the shells were dried at  $60^{\circ}C$  for 4  
133 hours and were then stored at ambient temperature until the biomechanical characterization.  
134

135 In the tensile and flexocompression tests, the scallop shells were respectively used in a  
136 wet condition, considering the same artificial seawater in which the shells were previously  
137 immersed (i.e., 33 PSU in salinity). All the material tested was previously reviewed by visual  
138 inspection in a compound microscope. If fractures were found, the leaflets were discarded,  
139 since they would not constitute a correct test and subsequent interpretation of the results.  
140 At the time of inspection, approximately 5% of the total samples showed significant cracks  
141 affecting the test results, which were discarded. In the tensile tests, the number of samples  
142 depends on the orientation. The minimum number of samples tested per group was two (2)  
143 in the  $0^{\circ}$  orientation in the 8.1 pH group and  $18^{\circ}C$  (all other groups were a minimum of  
144 four (4) samples per group).

145 For flexocompression tests five (5) full leaflets were used for each group, a total of 20 leaflets.

146 All animal care and experimental procedures were approved by the Ethics Committees  
147 of the Universidad Santo Tomás and the Universidad de Santiago de Chile (IE N° 0146), and  
148 they were conducted according to the Guide for the Care and Use of Laboratory Animals

149 published by the US National Institutes of Health (NIH Publication No. 85–23, revised  
 150 1996).

### 151 2.2. Tensile test

152 Tensile tests were performed on an Instron 3342 universal testing machine at a grip  
 153 test speed of 0.05 [mm/min]. The fabrication of the samples for the test was based on the  
 154 geometry of the ASTM E8/E8M standard [22] for flat samples and on the tests carried out  
 155 by Chen et al. [16], the main focus being on a reduced size and ultimate stress in the center of  
 156 the sample. The curvature of the shell must also be taken into account, so the samples were  
 157 taken from the outermost areas of the shell that present a similar age between specimens.  
 158 Figure 1 shows the generalities and basic dimensions of the samples for the tensile test.  
 159 There are three main directions to capture the anisotropy of the material subjected to this  
 160 stress ( $90^\circ$ ,  $0^\circ$  and  $45^\circ$ ) which is shown in Figure 1a. The initial transversal area  $A$  of each  
 161 specimen is estimated  $A = a \cdot b$  as can be seen in Figure 1b, where the dimensions  $a$  and  $b$   
 162 are measured with a micrometer (Mitutoyo  $\pm 0.005$  [mm]). The general set-up of the test  
 163 is shown in Figure 1c.

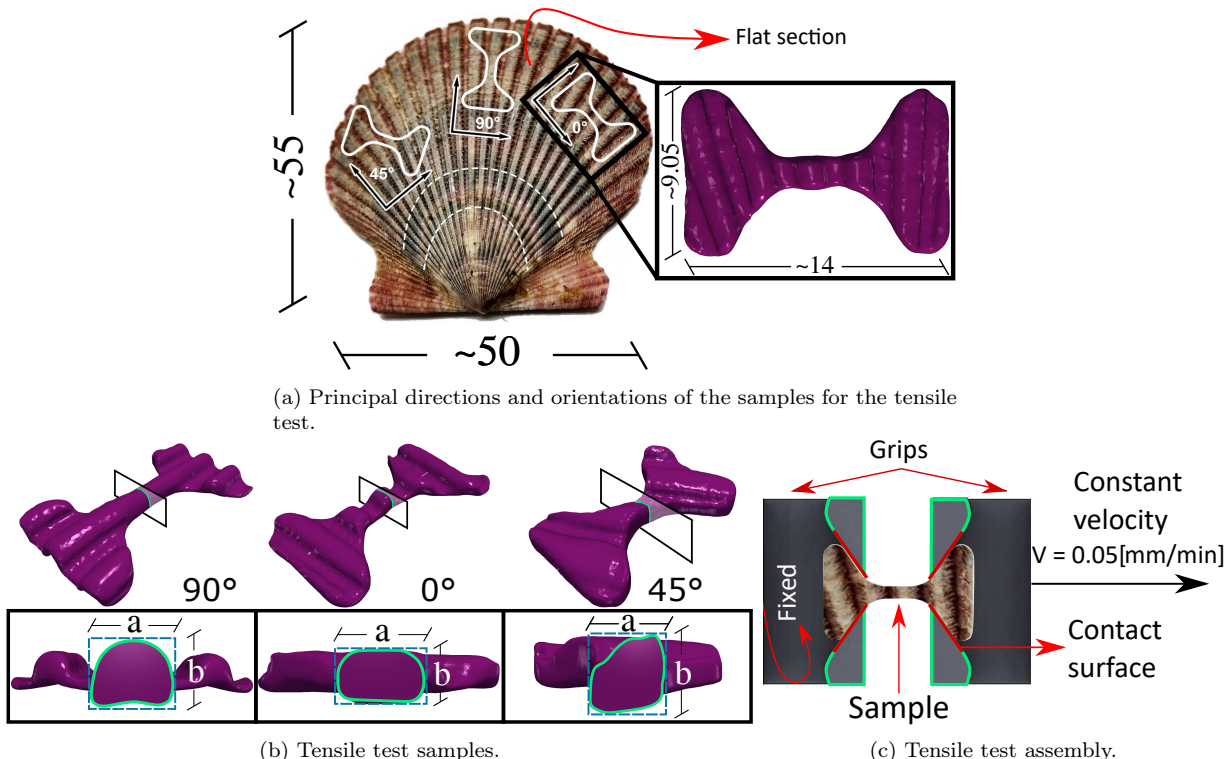


Figure 1: Specification for grips and samples for the tensile tests. Figure 1a shows the sample design for the tensile test, the principals directions and orientations of the samples. Figure 1b shows the cross sectional area of the samples and how its estimated. Figure 1c shows the tensile test assembly. All dimensions shown in mm.

164 A Dremel 3000 2/30 ACC multi-purpose cutting tool was used to manufacture the sam-  
 165 ples. The flat sections (Figure 1a) where then moved to a laser cutter (80 W nominal power)

166 at low power (20% capacity), cutting the shape of the sample using CAD/CAM technology.

167 *2.3. Flexocompression test*

168 Flexocompression tests were performed on an Instron 3342 universal testing machine at  
169 a punch test speed of 0.05 [mm/min]. The punch ( $\varnothing$  17 [mm]) was positioned at the top of  
170 the shell curve. The complete shell is positioned on a base with four supports, which was  
171 designed and manufactured in Ertacetal (high resistance polycarbonate) and machined with  
172 a CNC milling machine (Fanuc Saeil TNV-40). Figure 2 shows the design and configuration  
173 of the base for the flexocompression test.

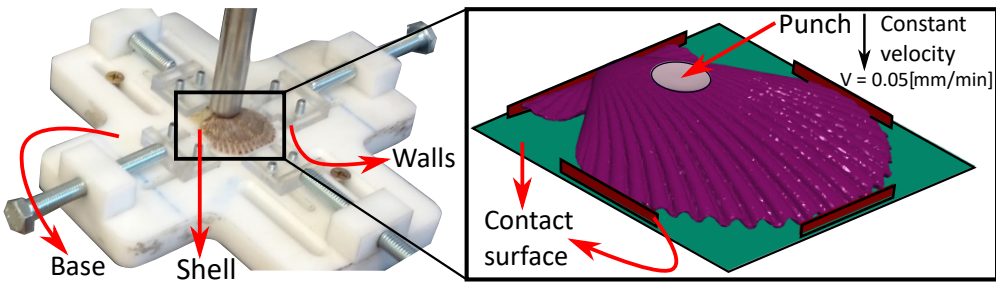


Figure 2: Flexocompression test configuration, showing the base for flexocompression test and the configuration of the test, in which the punch is located in the *umbo* of the shell (outer surface).

174 *2.4. Statistical methods*

175 All statistical analyses were carried out by means of a one-way analysis of variance  
176 (ANOVA). Assumptions of normality and homoscedasticity of the one-way ANOVA were  
177 evaluated using the Kolmogorov–Smirnov and Burtlett tests, respectively [23]. A significance  
178 of 0.05 was used to establish significant differences in the biomechanical properties of the  
179 individuals across treatments. The ANOVA analysis was followed by a Tukey test when  
180 there was the same number of samples in each group or treatment, or a Tukey-Kramer test  
181 when the number of data between the groups was different.

182 *2.5. Constitutive model*

183 Calcareous materials, such as bones, present viscoelastic and non-linear behaviour, how-  
184 ever, it is considered by a large number of authors as an anisotropic linear elastic material  
185 based on Katz and Meunier [24] research. This simplification of its behaviour depends on  
186 the stress to which it is submitted, where the quasi-static and non-impact process is valid  
187 [25]. Thus, the behaviour of hard tissues will be governed by the generalized Hooke's law  
188 written as:

$$\sigma = C \cdot \varepsilon \rightarrow \begin{Bmatrix} \sigma_1 \\ \sigma_2 \\ \sigma_3 \\ \tau_{12} \\ \tau_{23} \\ \tau_{13} \end{Bmatrix} = C \cdot \begin{Bmatrix} \varepsilon_1 \\ \varepsilon_2 \\ \varepsilon_3 \\ \gamma_{12} \\ \gamma_{23} \\ \gamma_{13} \end{Bmatrix} \quad (1)$$

189 where  $\sigma$  is the tension vector,  $C$  the stiffness, and  $\varepsilon$  the deformation vector. The relationship  
 190 shown in equation 1 is reversible, i.e.:

$$\varepsilon = C^{-1} \cdot \sigma \quad (2)$$

191 If the material has two or three orthogonal symmetrical axes, it is an orthotropic material,  
 192 where its elastic properties depend on the axis in which they are being measured. Following  
 193 symmetry considerations, the inverse stiffness matrix for an orthotropic material is given by:

$$C^{-1} = \begin{bmatrix} \frac{1}{E_1} & -\frac{\nu_{12}}{E_1} & -\frac{\nu_{13}}{E_1} & 0 & 0 & 0 \\ -\frac{\nu_{21}}{E_2} & \frac{1}{E_2} & -\frac{\nu_{23}}{E_2} & 0 & 0 & 0 \\ -\frac{\nu_{31}}{E_3} & -\frac{\nu_{32}}{E_3} & \frac{1}{E_3} & 0 & 0 & 0 \\ 0 & 0 & 0 & \frac{1}{G_{12}} & 0 & 0 \\ 0 & 0 & 0 & 0 & \frac{1}{G_{31}} & 0 \\ 0 & 0 & 0 & 0 & 0 & \frac{1}{G_{23}} \end{bmatrix} \quad (3)$$

194 As the stiffness matrix is symmetrical, then there are 12 elastic constants:

- 195 • Elastic modulus:  $E_1$ ,  $E_2$  and  $E_3$ .
- 196 • Poisson's ratio:  $\nu_{12}$ ,  $\nu_{13}$ ,  $\nu_{21}$ ,  $\nu_{23}$ ,  $\nu_{31}$  and  $\nu_{32}$ .
- 197 • Shear modulus:  $G_{12}$ ,  $G_{13}$  and  $G_{23}$ .

198 where 9 of these constants are independent:  $E_1$ ,  $E_2$ ,  $E_3$ ,  $\nu_{12}$ ,  $\nu_{13}$ ,  $\nu_{23}$ ,  $G_{12}$ ,  $G_{13}$  and  $G_{23}$ .  
 199 These values can be obtained by tensile tests with samples cut in various directions.

200 For the estimation of the Poisson ratios, a value of 0.2 will be used in all directions based  
 201 on the research of Blau and Davis [26] for non-ferrous materials. The shear modulus is esti-  
 202 mated for each orientation using the relationship proposed by Huber [27, 28] for orthotropic  
 203 materials in their linear elastic zone:

$$G_{ij} = \frac{\sqrt{E_i E_j}}{2(1 + \sqrt{\nu_{ij} \nu_{ji}})} \quad (4)$$

## 204 2.6. Numerical simulations

205 To perform a numerical fitting of the parameters obtained experimentally by the me-  
 206 chanical tests, numerical simulations of them are made using the finite element method  
 207 (FEM) and then the results are analyzed following the same procedures and experimental  
 208 methodologies described above. One of the problems described by several authors is the  
 209 complex geometry of the shells, so it was decided to use microCT scans with high enough  
 210 accuracy (Bruker Skyscan 1278) to acquire the important structural details. Thus, full-shell  
 211 geometries and tensile specimens in the three different orientations were obtained with an  
 212 accuracy of 50 microns. The scanned specimens are of the same age and growth groups as  
 213 the experimental samples. All simulations were carried out using VULCAN, an FEA software  
 214 developed in-house.

215    2.6.1. Coordinate system of elements

216    Considering the shell as a material of orthotropic behavior [24], and due to the complex  
 217    geometries present in the experimental tests carried out, it is necessary to represent such  
 218    characteristic in the numerical simulations where when using FEM it is necessary to adjust  
 219    the coordinate system of every element of the mesh according to the orthotropy. In order  
 220    to achieve these requirements, a method was developed that is capable of considering the  
 221    geometry of the shell from its barycenters, and using parameterized surfaces, to represent  
 222    the three directions of the orthotropic behavior of all the geometry, extrapolating in a  
 223    particular way the behavior to each element. The process requires, in the first instance,  
 224    meshing the solid, either the shell or the tensile specimen, and obtaining the barycentre of  
 225    the tetrahedral element that forms the mesh of the solid, which serves as a reference for the  
 226    geometric location of the element. After obtaining the barycentres, the project "The Point  
 227    Cloud Library (PCL)" [29], an open-source library of algorithms for point cloud processing  
 228    tasks and 3D geometry processing, is used. Such application was modified in such a way  
 229    that the barycenters represent the point cloud, and from these data, it is possible to run  
 230    the B-spline fitting algorithm on this point-cloud, to obtain a smooth, parametric surface  
 231    representation. Assume that a surface has a parametric form  $\Gamma : \mathbf{s}(u, v)$  in  $\mathbb{R}^3$ , the editing  
 232    of the program consists of selecting at the same time the parameters for B-spline Surface  
 233    fitting (the refinement of the surface and the number of iterations), and visualizing each  
 234    step of the refinement and iteration until the surface is adapted to the point cloud, as can  
 235    be seen in Figure 3.

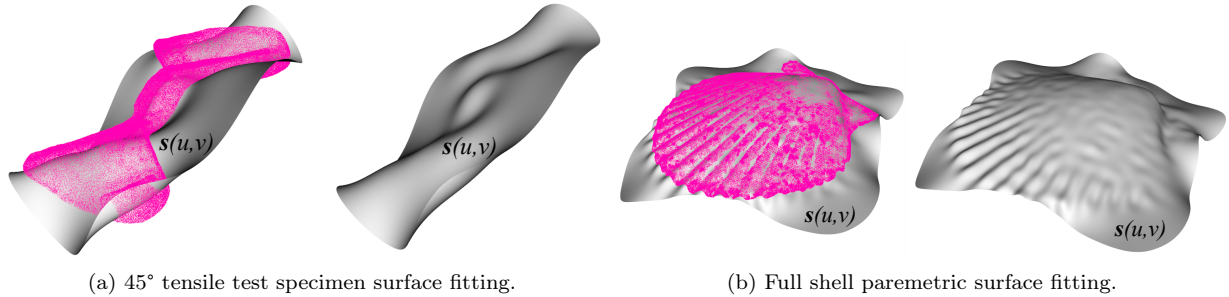


Figure 3: Parametric surfaces adjusted to the barycentres of meshes for 45° tensile and full shell specimens.

236    Once a parametric surface has been fitted to the meshes, the normal direction to the  
 237    surface is obtained, the first of the three orthogonal directions. To compute the normal  
 238    directions of all the elements it is necessary to calculate the orthogonal projection from  
 239    the barycentre to the surface, and the used method that manages to do this operation,  
 240    which considers a great speed due to the abundant amount of points, that does not have  
 241    convergence problems and that is independent of the initial iteration value (i.e. not using  
 242    Newton's method), is the work carried out by Li et al. [30], which computes the minimum  
 243    distance between a point and a parametric surface, and then to return the nearest point  
 244    (foot point) on the surface as well as its corresponding parameter, which is also called the  
 245    point projection problem of a parametric surface, the GSA method. Subsequently, it is  
 246    possible to create a vector that goes from the foot point, created from the GSA method, to

247 the barycenter and, in this way, all barycenters, which represent the tetrahedral elements of  
 248 the solid, have their respective direction normal to the surface. The other two directions are  
 249 obtained considering the point of origin of the growth lines, which is used to create a vector  
 250 that goes from that point of origin to all the barycenters of the figure, so that with a simple  
 251 cross product it is possible to calculate the directions longitudinal to the growth lines and  
 252 transversal to it, as can be seen in Figure 4.

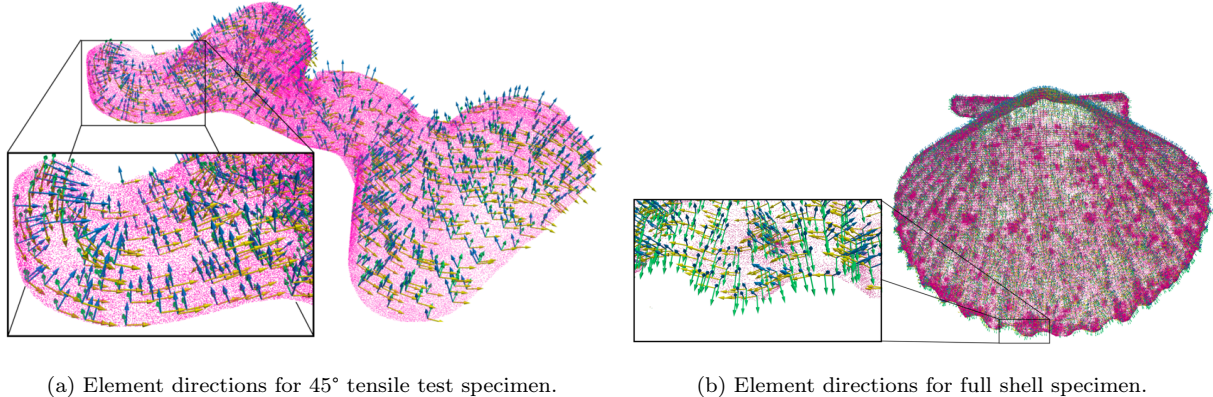


Figure 4: Element directions fitting for meshes used in FEM simulations. In the boxes is shown the orientations of the particular coordinated system in relation to an global orthotropic behavior.

### 253 2.6.2. Tensile test

254 The simulation of the tensile test considers the three specimen geometries according to  
 255 their direction (90, 0 and 45°) which will behave, hypothetically, following an orthotropic  
 256 linear elastic model. The calculation of the cross sectional area its the same followed ex-  
 257 perimentally, described in Figure 1b. The specimen grip will act as a rigid surfaces on the  
 258 specimen and the contact model used (a complete description of the contact penalty method  
 259 is described by Cañas et al. [31]), considers that the contact pressure ( $p_n$  [MPa]) increases  
 260 quadratically with the penetration ( $g_n$  [mm]) of the surfaces, i.e.:

$$P_n = E_{n0}g_n + E_ng_n^2 \quad (5)$$

261 where  $E_{n0}$  [N/mm<sup>3</sup>] and  $E_n$  [N/mm<sup>4</sup>] are constants that control the penetration. Due to the  
 262 high number of simulations, a code was developed to automatically adjust these constants to  
 263 avoid excessive penetrations and erroneous results. These simulations will be used to adjust  
 264 the elastic parameters numerically, as explained below.

### 265 2.6.3. Flexocompression test

266 The numerical simulation of this test, which will be used for the validation of the tests  
 267 and adjusted results, has the complete shell with a linear elastic orthotropic material and  
 268 several surfaces that will have contact with the specimen. These contacts respond to the  
 269 different planes that interact with the specimen, restricting its displacement or applying  
 270 force, as shown experimentally in Figure 2. The contact model used is shown in equation 5.

271 2.6.4. Fitting procedure

272 Having adopted the orthotropic linear elastic model (section 2.5), and considering the  
 273 large number of parameters involved in it, a proper fit strategy must be adopted through  
 274 numerical simulations. This is how, and according to Figure 5, we follow an iterative  
 275 process until a minimum error criterion is satisfied in relation to the experimental data.

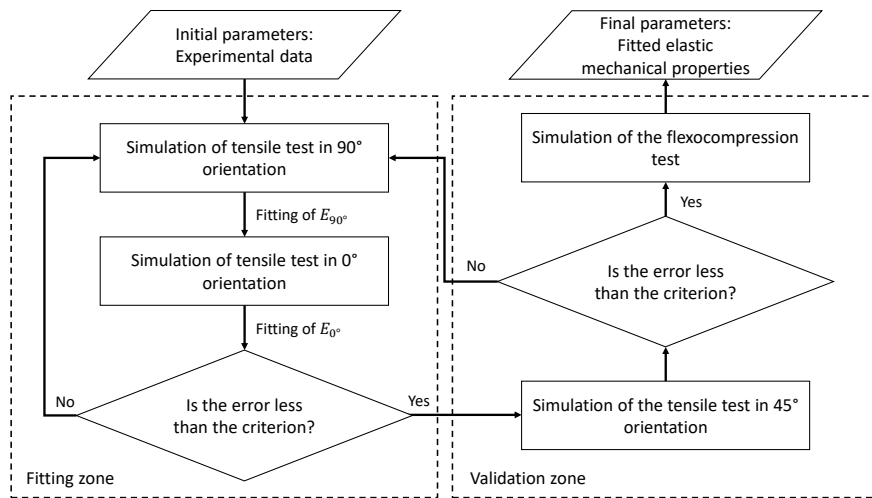


Figure 5: Flowchart of the fitting procedure of elastic properties through numerical simulations.

276 Figure 5 represents how the numerical fitting of the properties obtained experimentally will  
 277 be done, so they will be the input data for the numerical simulations, and the following  
 278 steps will be done until a satisfactory adjustment is achieved.

279

280 **Step 0.** With the experimental properties, and considering an orthotropic behavior, it is  
281 that they are coupled to the tensile models and the simulations are started. The shear  
282 modulus will be calculated according to Huber's equation [27], as explained above.

283  
284 **Step 1.** Tensile simulations are run at 90° and 0° to obtain the resulting force on a pair  
285 of cooperative grip contact surfaces. The same experimental methodology will be followed  
286 to obtain the behavior of the specimen in strain versus stress and thus the elastic modulus,  
287 which will be adjusted in relation to the initial experimental one. This step is repeated until  
288 the error criteria are satisfied, explained below.

289  
290 **Step 2.** Once the error criteria for the 90° and 0° simulations have been satisfied, these  
291 results are validated by performing the 45° tensile simulation. If the error exceeds the  
292 chosen criterion, the fittings performed will be reanalysed. If the error is lower (compared to  
293 the experimental results), the process of adjusting the model from the perpendicular plane  
294 stiffnesses has been validated.

295  
296 **Step 3.** With the elastic properties adjusted numerically, the simulation of the flexocom-  
297 pression test is carried out, where the shell will be engaged in the area of the *umbo* by a  
298 cylindrical punch with a convex head, with a geometry similar to that used experimentally.  
299 The results are compared with those obtained in the tests to observe the behavior of the  
300 final adjusted mechanical elastic properties of the material to validate the mechanical tests.

301  
302 The error for each step of data fitting in the numerical simulation is quantified by means  
303 of the normalized root-mean-square deviation (NRMSD) in order to obtain a comparable  
304 value with the experimental curve. This parameter is defined by the equation 6.

$$\text{NRMSD} = \frac{1}{\Delta} \sqrt{\frac{1}{n} \sum_{i=1}^n (y_i - \hat{y}_i)^2} \quad (6)$$

305 where  $n$  is the number of experimental data,  $y_i$  are the experimental measures,  $\hat{y}_i$  is the  
306 adjusted numerical value, and  $\Delta$  is defined as shown in the equation 7.

$$\Delta = |y_{max} - y_{min}| \quad (7)$$

307 To obtain the NRMSD in this particular case, the values to be considered in  $y$  is the measure  
308 of engineering stress, both experimental and numerical, at the same point of engineering  
309 strain at each spot. The adjustment of the mechanical properties will be made until the  
310 NRMSD, our criterion error, are less than 8%. The magnitude of this criterion was chosen  
311 considering possible geometrical problems resulting from different sizes with the experiments,  
312 which could generate divergences in the adjustments with smaller criteria.

<sup>313</sup> **3. Results and discussion**

<sup>314</sup> *3.1. Experimental tests*

<sup>315</sup> *3.1.1. Tensile test*

<sup>316</sup> The tensile test described how the sample is placed in the grips, which is shown as a  
<sup>317</sup> little curve at the beginning of the force versus displacement curve. Then, for the analysis of  
<sup>318</sup> the mechanical behavior, the linear elastic section is considered, i.e., where there is a real  
<sup>319</sup> load in the tensile sample. The bending stresses are applied to the samples due to the small  
<sup>320</sup> curvatures along their length, which is one of the reasons why a numerical fitting of these  
<sup>321</sup> results should be made as they are not completely standard test pieces.

<sup>322</sup>  
<sup>323</sup> Once the force versus displacement curve data have been split, the engineering stress ( $\sigma$ )  
<sup>324</sup> versus engineering strain ( $\varepsilon$ ) curves will be calculated from the initial dimensions of each  
<sup>325</sup> sample and the distance between grips at the start of the test. In each experimental test,  
<sup>326</sup> a linear fitting will be made using the least squares method, thus obtaining the apparent  
<sup>327</sup> elastic modulus ( $E$ ) of each test. Therefore, the ultimate stresses and deformations and the  
<sup>328</sup> apparent elastic modulus for each group analyzed will be obtained. The results are shown in  
<sup>329</sup> Figure 6. The results are described as apparent based on the calculation of the area and the  
<sup>330</sup> complex geometry of each specimen, as can be seen in Figure 1b, which would not directly  
<sup>331</sup> result in stress, strain and elastic modulus, leading directly to evaluate and correct the  
<sup>332</sup> results using numerical simulations with the adopted orthotropic model. Notwithstanding  
<sup>333</sup> the above, a statistical analysis to the uncorrected values to evaluate differences between  
<sup>334</sup> groups would not be incorrect to perform, since the adjustment of elastic parameters is  
<sup>335</sup> considered similar between all of them, as the geometry between specimens is similar.

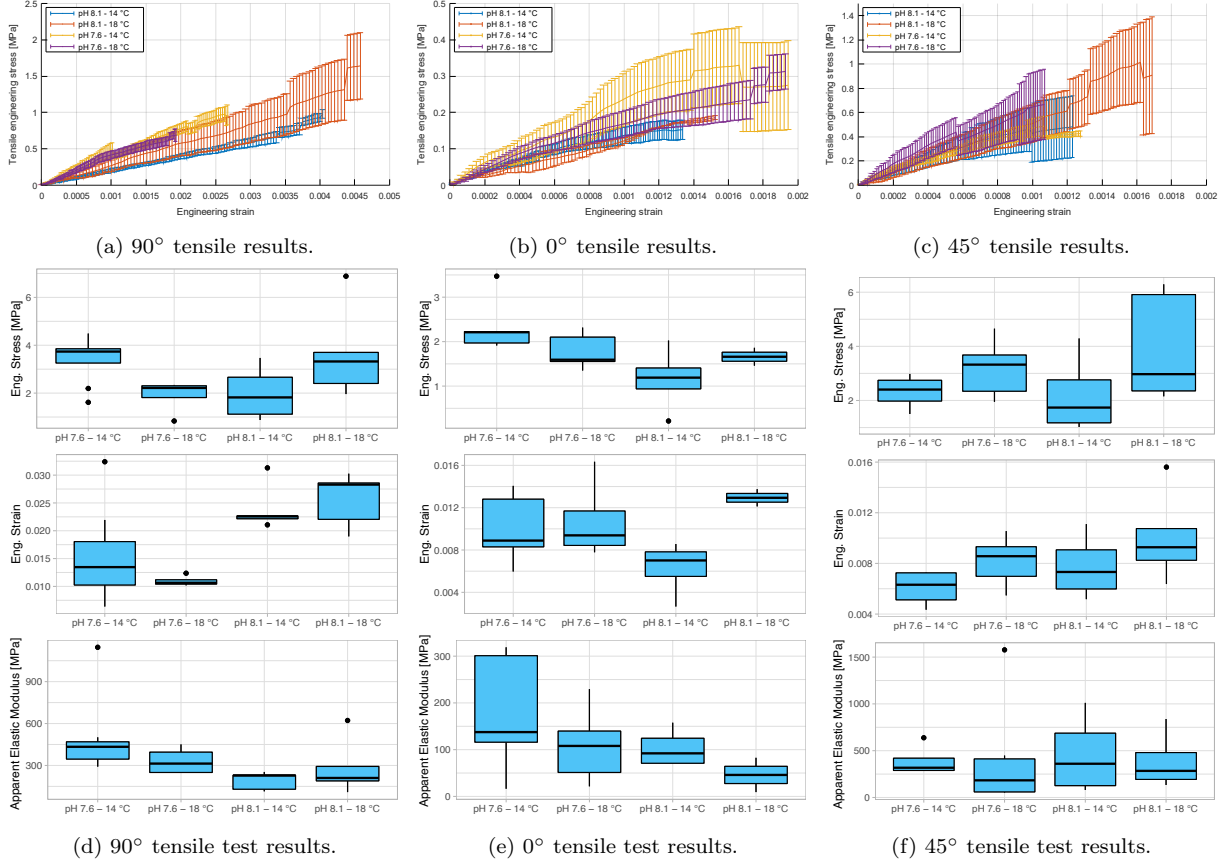


Figure 6: Results of the tensile test apparent behavior in engineering stress ( $\sigma$ ) against engineering strain ( $\epsilon$ ). Figures 6d, 6f, 6e show a comparison of the mechanical behavior on the maximum strain, maximum engineering stress, and the elastic modulus. (●): extreme values of the distribution.

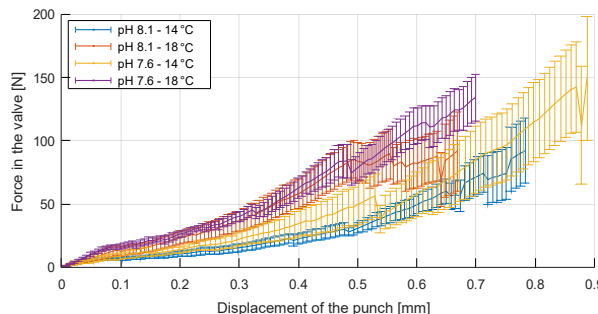
The mechanical tensile behavior of all groups varies with their orientation. The longitudinal (90°) and transverse (0°) orientations are the ones that present the greatest differences, the response to 0° being much weaker. In addition, for all directions a linear response is observed with the deformation. The anisotropic and linear mechanical response of this material is consistent with the preferential orientation of the crystals that has been reported by Taylor and Layman [14]. After statistically analyzing the results of the tensile test it is seen that for the transverse orientation (0°) there are no significant differences between variables measured at all, considering variances and means.

These results are different from those presented by Abarca [20] in the compression behavior where it shows significant differences in the elastic modulus between the pH 7.6 and 14°C group and all the others, including the control, wet condition, and compression in the thickness. The above indicates anisotropic behavior in compression with significantly different properties from each other, so that, even if there are no significant differences between directions in the tensile tests, they will be considered as independent elastic properties for the orthotropic model. Not having significant differences between groups both in stiffness,

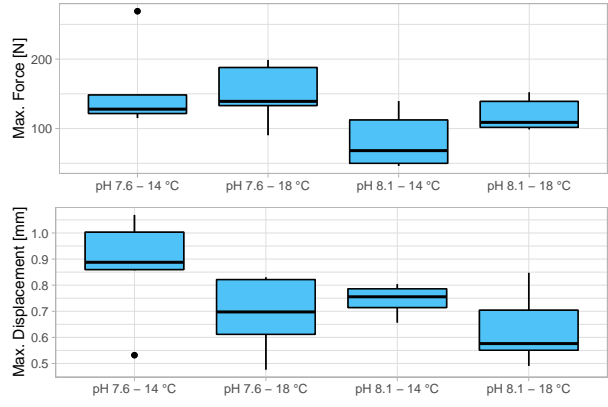
as in strains or maximum stresses, indicates that the animal adapts to different scenarios of growth to which it is subjected, at least in its juvenile stage before reaching maturity. This adaptation responds to an increase in its metabolism and change in the crystalline composition in order to maintain mechanical properties in hostile environments, as Ramajo et al. [10] and Lardies et al. [9] wrote on their researches. These findings support the hypothesis of biomineralization plasticity as a potentially advantageous compensatory mechanism, as described by Leung et al. [32] and Telesca et al. [33].

### 3.1.2. Flexocompression test

Figure 7a shows a representative force curve in the shell against punch displacement when it is in contact with the shell. The four groups up to the fracture are shown and a non-linear behavior is seen at this forced state. This is related as stated by Checa et al. [34] who describes an arrangement of crystals in the microstructure of shells of mollusks as they are fractured in a quasi-static flexion.



(a) Force against displacement graph.



(b) Maximum force and displacement.

Figure 7: Figure 7a show the behavior of complete shells in flexocompression test. It is shown at the application of force on the shell and displacement of the punch (vertical) in the umbo. Figure 7b show the comparison of the behavior of shells subjected to flexocompression tests. The top graph shows the maximum force applied to the shell [N] and the bottom graph shows the displacement of the punch [mm] before the fracture. (•): extreme values of the distribution.

The minor breaks seen in Figure 7a are due to the fact that there are cracks in the material but these are not catastrophic at the end of the test, i.e. the material can withstand the cracks produced. If the cracks have occurred under natural conditions (pH 8.1 / 14°C), the animal can recover the damaged material if it has the corresponding food and if the crack is not big enough for the predator to have access to the mollusk's muscle [34]. The material has a fragile behavior, where when passing the elastic zone a sudden break is produced, which represents the critical fracture of the shell. The maximum punch displacement and maximum shell force are shown in Table 1, and it can be seen in the boxplot in Figure 7b.

Condition	Force on shell [N]	Displacement of the punch [mm]
pH 8.1 - 14 °C	$83.31 \pm 18.32$	$0.74 \pm 0.03$
pH 8.1 - 18 °C	$120.20 \pm 10.71$	$0.63 \pm 0.06$
pH 7.6 - 14 °C	$156.45 \pm 28.67$	$0.87 \pm 0.09$
pH 7.6 - 18 °C	$149.90 \pm 19.69$	$0.69 \pm 0.07$

Table 1: Maximum values for the behaviour of shells in the flexocompression test. Mean and standard error of force and displacement.

According to the analysis of variance, there are no significant differences between groups for variables of forces and displacement ( $p > 0.05$ ). Therefore, the variation of pH and temperature applied to the group and control does not produce significant differences for the flexocompression test in the variables of displacement and force. These results are in line with what was described above, where the animal is able to adapt to changes in its juvenile stage to achieve mechanical properties that are not unfavorable to predation. Therefore, a compensatory mechanism, such as biomineralogical plasticity, may be working under OA conditions [32, 33].

### 3.2. Numerical simulations

The results of the experimental tests obtained indicate that there are no significant differences between groups for their tensile elastic properties, so the numerical simulations will focus on the control group (pH  $\sim 8.1$  and 14°C) being representative of the expected behavior. On the other hand, it is interesting to compare what was obtained in tensile tests with the compression properties reported by Abarca [20], as, in magnitude, there is a difference close to 82% (based on a relative error centered on the compression properties) which could give signs of bimodular behaviour, so, focused on the fitting process in tensile test, this factor will be evaluated.

#### 3.2.1. Tensile test

Using the orthotropic model described in section 2.5, the experimental tensile tests are simulated based on the results obtained, using as input variables the elastic modulus in the longitudinal (90°) and transversal (0°) directions, while for the direction in the thickness, it is used what is reported by Abarca [20], to compression, for the same group ( $E_z = 131.28$  MPa). After a series of iterations following the process described in Figure 5, an expected error criterion of less than 8% was achieved, results that are shown in Figure 8 for the simulations to tensile in its longitudinal and transversal directions. The validation is carried out with the simulation in diagonal direction (45°) obtaining a very small error in relation to the experimental curve (around 2%) having only fitted the elastic properties in the plane. Table 2 shows the results obtained compared to the unfitted ones, in addition to showing the NRSMD for each direction.

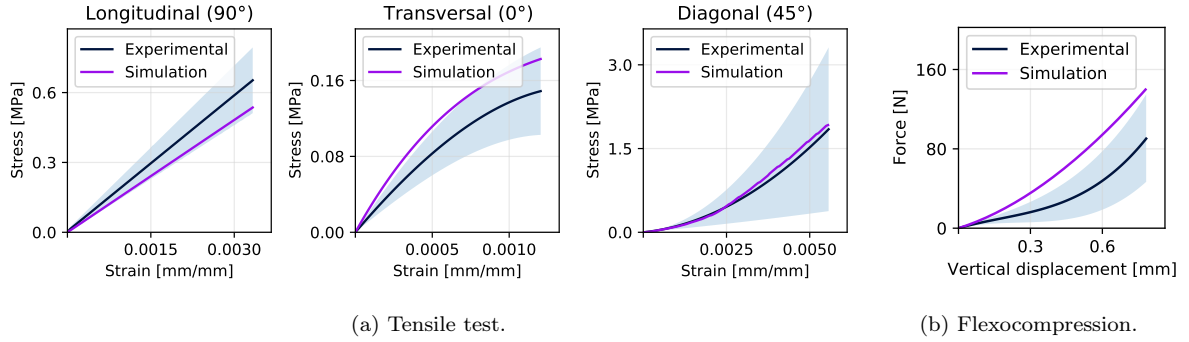


Figure 8: Results of simulations and comparison with experimental tests. Figure 8a shows the simulation results of the tensile test, both for the elastic properties fitting stage (longitudinal and transversal direction) and for the validation stage (diagonal). Figure 8b shows the validation of the orthotropic model adopted with the adjusted properties obtaining an error of approximately 23%.

Direction	Initial E.M. [MPa]	Final E.M. [MPa]	NRSMD
Longitudinal (90°)	199.156	407.947	2.59%
Transversal (0°)	57.524	143.633	7.78%

Table 2: The table shows the results of the unfitted experimental elastic properties and the fitted elastic properties obtained from the tensile test and their respective fit.

Considering the results obtained in the fitting process of elastic properties and in comparison to those reported by Abarca [20] in compression tests and in the same orthotropic directions of our tensile tests, it is that, although after adjusting the elastic modules in the Longitudinal (90°) and Transverse (0°) directions, these increase considerably their stiffness, they do not become sufficiently close to the compression properties, reaching relative differences close to 62.5% in the Longitudinal case, as is shown in the table 3. Therefore, it can be said that if a shell is to be completely known and characterized by these characteristics, the properties of both compression and tension must be known and a comparative study carried out between them.

Direction	Compression E.M [MPa]	Final E.M [MPa]	Diff.
Longitudinal (90°)	1080.287	407.947	62.2%
Transversal (0°)	226.362	143.633	36.5%
Thickness	131.277 [20]	—	—

Table 3: The table shows the results in comparison to the properties reported by Abarca [20] of uniaxial compression tests in the three orthogonal directions in comparison to those obtained from the tensile test, both experimental and its fitting as well as the difference obtained between both calculated as percentage relative error.

### 3.2.2. Flexocompression test

After the validation of the tensile test simulation in the diagonal direction (45°), the numerical simulation of the flexocompression test is carried out. The same set-up of the

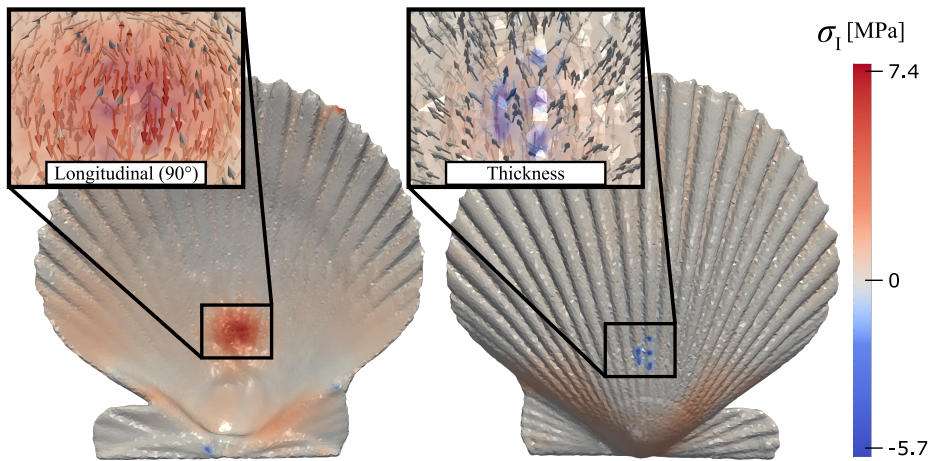
414 experimental test is used (Figure 2), in which the punch, base and walls were implemented  
 415 by means of quadratic contact elements; the shell was meshed using tetrahedral elements.  
 416 The mechanical properties obtained by fitting the simulations of the tensile tests were those  
 417 implemented for this case in a unimodular orthotropic model, according to the process  
 418 described in Figure 5. The results of the simulation, in comparison with the experimental  
 419 results of the flexocompression test, is shown in Figure 8b where a similar behavior can  
 420 be observed between both studies, obtaining a quantifiable error of 23.33%. Although this  
 421 error exceeds what was proposed as a criterion for fitting of the elastic properties, and  
 422 considering that this test was simulated as part of the validation of the problem, in addition  
 423 to the particular individual geometry of each of the shells, which will be irremediably differ-  
 424 ent from each other and therefore will present different levels of contact and non-linearity  
 425 (shell-surface contact zone), it is considered that the error obtained is acceptable to validate  
 426 the results.

427  
 428 The simulation analysis is focused on the stress concentration in the area where the  
 429 punch contacts the shell; by mapping the principal stresses  $\sigma_I$ ,  $\sigma_{II}$  and  $\sigma_{III}$  in the shell-  
 430 punch contact zone (Figure 9). An interesting effect is observed, an approximate alignment  
 431 between the directions of the principal stresses and the three orthotropic directions of the  
 432 material, which occurs both on the outer (compression) and inner (tension) surface of the  
 433 shell. The corresponding alignments for the outer and inner surface are shown in Table 4.

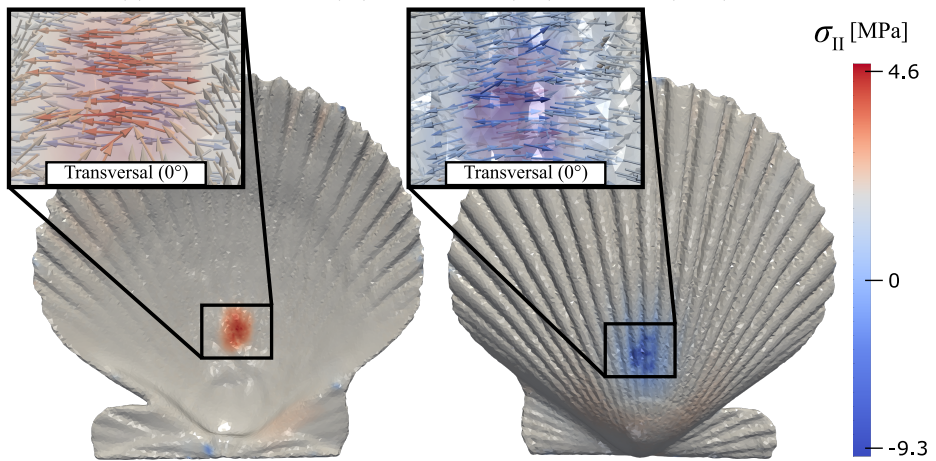
Zone	Principal stresses $\sigma_I$ $\sigma_{II}$ $\sigma_{III}$		
Outer (Compression)	$\sigma_I \rightarrow$ Thickness	$\sigma_{II} \rightarrow$ Transversal	$\sigma_{III} \rightarrow$ Longitudinal
Inner (Tension)	$\sigma_I \rightarrow$ Longitudinal	$\sigma_{II} \rightarrow$ Transversal	$\sigma_{III} \rightarrow$ Thickness

Table 4: Alignment between principal stresses directions ( $\sigma_I$ ,  $\sigma_{II}$  y  $\sigma_{III}$ ) and orthotropic directions (Longitudinal, Transversal and Thickness) in the shell-punch contact area produced by the effects of compressive stresses (outer surface) and tensile stresses (inner surface), as shown in Figure 9.

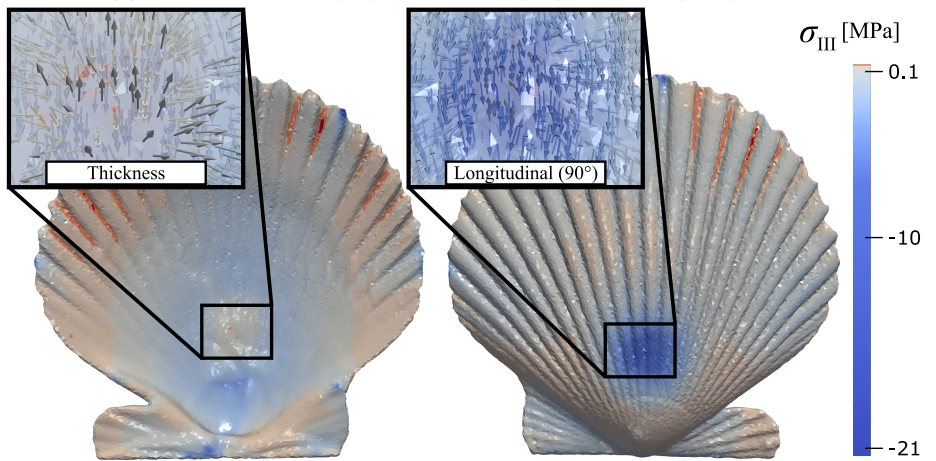
434 The highest magnitudes of tensile and compressive stress in the shell-punch contact zone  
 435 were distributed in the longitudinal direction, i.e. in the directions parallel to the ribs,  
 436 which have a higher inertia compared to the rest of the shell. In addition, the compressive  
 437 stress exceeds the tensile stress, which indicates that under predation attacks the shell must  
 438 withstand this stress to ensure the survival of the mollusk.



(a) Principal Stress I ( $\sigma_I$ ) on the inner (left) and outer (right) surface.



(b) Principal Stress II ( $\sigma_{II}$ ) on the inner (left) and outer (right) surface.



(c) Principal Stress III ( $\sigma_{III}$ ) on the inner (left) and outer (right) surface.

Figure 9: Principal stresses magnitude and directions (in the boxes) in the shell-punch contact area.

439 **4. Conclusions**

440 This research was devoted to the characterization of the mechanical behavior of scallops  
441 shells subjected experimentally to climate change scenarios for the ocean (acidification and  
442 warming). Special devices were designed and manufactured to quantify mechanical proper-  
443 ties of mollusk shell material in quasi-static tests. The methods developed and explained in  
444 the present work, can be further applied to different species in order to characterize their  
445 biomechanical properties. The effect on the mechanical behaviour of shells during growth  
446 conditions under climate change scenarios has been studied.

447 In general, the groups with the best mechanical properties (more resistant and stiffer)  
448 were those that grew at a high temperature (18°C), this variable turning out to be the most  
449 sensitive in the behaviour of the material. Temperature and pH alterations lead to different  
450 levels of calcification that might be related to a biomechanical adaptation process due to  
451 climate change scenarios, a process in line with mineralogical plasticity as a compensatory  
452 mechanism to the impacts of ocean acidification [32, 33]. Mechanical anisotropies were  
453 found according to the orientation at which they were performed, similar to previous studies  
454 [20]. It was found, after performing tensile tests and their respective parameter fittings and  
455 validation, that the shell behaves according to an orthotropic unimodular model. However,  
456 and according to the results shown in the present study, if one wants to know in depth the  
457 macromechanical behavior of this class of bivalves it is imperative to study the behavior in  
458 compression as well as in tension. Scallop shells (*AP*), as they become stiffer and more resis-  
459 tant under conditions of acidity and high temperature indicate some adaptation to extreme  
460 controlled environments, but nevertheless, they can also affect the energy distribution they  
461 have to achieve greater growth or a more efficient shape for their aquatic transport. If the  
462 condition of high acidity and temperature occurs in a natural environment, the scallop food  
463 (protozoa, larvae of other organisms, and algae) will also be affected and reduced, so its  
464 chances of surviving without being in artificial hatcheries are significantly reduced. Other  
465 factors related to climate change need to be evaluated in further studies.

466  
467 Therefore, and considering the results obtained in the present study, it can be said that  
468 for *AP* it is validly mechanically modeled with a unimodular orthotropic model, where the  
469 directions of the main stresses to which it is subjected are directly related according to its  
470 crystalline microstructure (Lagos et al). submitted. This is significant due to the survival  
471 mechanisms that the animal is able to develop under mechanical loads, allowing us to know  
472 the direction and orientation in which the shell concentrates the main stresses. Similarly,  
473 with this knowledge it is possible to develop tools to avoid the concentration of stresses  
474 in those directions in industrial processes in order to obtain less loss of material in the  
475 harvesting stage of the mollusk.

476

477 **Conflicts of interest**

478 The authors have no conflicting interests regarding this paper.

479 **Acknowledgements**

480 The supports provided by the PIA ANILLOS ACT project No. 172037 of the Chilean  
481 Council for Research and Technology (ANID - Ex CONICYT), and the FONDEQUIP  
482 project EQM150010 of ANID are gratefully acknowledged. In addition, we thank the  
483 support provided by DICYT from the Universidad de Santiago de Chile and by ANID  
484 PFCHA/DOCTORADO BECAS CHILE/2019 – CEL00011051.

485 **References**

- 486 [1] C. Sabine, R. Feely, and N. Gruber. The oceanic sink for anthropogenic co<sub>2</sub>. *Science*, 305:367–371,  
487 2004.
- 488 [2] T. Wigley, R. Richels, and J. Edmonds. Economic and environmental choices in the stabilization of  
489 atmospheric co<sub>2</sub> concentrations. *Nature*, 379:240–243, 1996.
- 490 [3] D. Wolf-Gladrow, U. Riebesell, S. Burkhardt, and J. Bijma. Direct effects of co<sub>2</sub> concentration on  
491 growth and isotopic composition of marine plankton. *Tellus B. Chemical and Physical Meteorology*, 51:  
492 461–476, 1999.
- 493 [4] R. Torres and P. Ampuero. Strong co<sub>2</sub> outgassing from high nutrient low chlorophyll coastal waters off  
494 central chile (30°s): The role of dissolved iron. *Estuarine, Coastal and Shelf Science*, 83(2):126 – 132,  
495 2009. ISSN 0272-7714.
- 496 [5] R. Feely, C. Sabine, J. Hernandez-Ayon, D. Ianson, and B. Hales. Evidence for upwelling of corrosive  
497 “acidified” water onto the continental shelf. *Science*, 320(5882):1490–1492, 2008. ISSN 0036-8075.
- 498 [6] N. Gruber, C. Hauri, Z. Lachkar, D. Loher, T. Frölicher, and G. Plattner. Rapid progression of ocean  
499 acidification in the california current system. *Science*, 337(6091):220–223, 2012. ISSN 0036-8075.
- 500 [7] A. Barton, B. Hales, G. Waldbusser, C. Langdon, and R. Feely. The Pacific Oyster, *Crassostrea gigas*,  
501 shows negative correlation to naturally elevated carbon dioxide levels: implications for near-term ocean  
502 acidification effects. *Limnol Oceanogr.*, 57:698–710, 2012.
- 503 [8] N. Lagos, S. Benítez, C. Duarte, M. Lardies, B. Broitman, C. Tapia, P. Tapia, S. Widdicombe, and  
504 C. Vargas. Effects of temperature and ocean acidification on shell characteristics of Argopecten purpu-  
505 ratus: implications for scallop aquaculture in an upwelling-influenced area. *Aquaculture Environment  
506 Interactions*, 8(Ipc 2014):357–370, 2016. ISSN 1869-215X. doi: 10.3354/aei00183.
- 507 [9] Marco A. Lardies, Samanta Benitez, Sebastian Osores, Cristian A. Vargas, Cristián Duarte, Karin B.  
508 Lohrmann, and Nelson A. Lagos. Physiological and histopathological impacts of increased carbon  
509 dioxide and temperature on the scallops argopecten purpuratus cultured under upwelling influences  
510 in northern chile. *Aquaculture*, 479:455 – 466, 2017. ISSN 0044-8486. doi: <https://doi.org/10.1016/j.aquaculture.2017.06.008>. URL <http://www.sciencedirect.com/science/article/pii/S0044848616312996>.
- 512 [10] Laura Ramajo, Carolina Fernández, Yolanda Núñez, Paz Caballero, Marco A Lardies, and María Jose-  
513 fina Poupin. Physiological responses of juvenile chilean scallops (argopecten purpuratus) to isolated  
514 and combined environmental drivers of coastal upwelling. *ICES Journal of Marine Science*, 76(6):  
515 1836–1849, May 2019. doi: 10.1093/icesjms/fsz080. URL <https://doi.org/10.1093/icesjms/fsz080>.
- 517 [11] E. M. Harper. Are calcitic layers an effective adaptation against shell dissolution in the bivalvia? *Journal of Zoology*, 251(2):179–186, 2000.
- 518 [12] Frédéric Marin, Gilles Luquet, Benjamin Marie, and Davorin Medakovic. Molluscan shell proteins:  
519 Primary structure, origin, and evolution. In *Current Topics in Developmental Biology*, volume 80  
520 of *Current Topics in Developmental Biology*, pages 209 – 276. Academic Press, 2007. doi: [https://doi.org/10.1016/S0070-2153\(07\)80006-8](https://doi.org/10.1016/S0070-2153(07)80006-8).
- 522 [13] O. B. Bøggild. The shell structure of the mollusks. *Det Kongelige Danske Videnskabernes Selskabs  
523 Skrifter. Naturvidenskabelig og Mathematisk Afdeling, Raekke 9*, 2:231–326, 1930. URL <https://ci.nii.ac.jp/naid/20000946111/en/>.
- 525 [14] J. Taylor and M. Layman. The mechanical properties of bivalve (Mollusc) shell structures. *Paleontology*,  
526 16:73–87, 1972.

- 527 [15] J.G. Carter. *Skeletal Biomineralization: Patterns, Processes and Evolutionary Trends: Volume II. Atlas and Index*. Springer, 2013. ISBN 1489953930.
- 528 [16] Guowei Chen, Hongyun Luo, Shunfei Luo, Zhenying Lin, and Yue Ma. Vertically oriented structure and its fracture behavior of the Indonesia white-pearl oyster. *Journal of the Mechanical Behavior of Biomedical Materials*, 66:211–223, 2016. doi: 10.1016/j.jmbbm.2016.11.002.
- 529 [17] Yuan Meng, Zhenbin Guo, Haimin Yao, Kelvin W.K. Yeung, and V. Thiagarajan. Calcium carbonate unit realignment under acidification: A potential compensatory mechanism in an edible estuarine oyster. *Marine Pollution Bulletin*, 139:141–149, feb 2019. doi: 10.1016/j.marpolbul.2018.12.030. URL <https://doi.org/10.1016/j.marpolbul.2018.12.030>.
- 530 [18] Aurélie Dery, Marie Collard, and Philippe Dubois. Ocean acidification reduces spine mechanical strength in euechinoid but not in cidaroid sea urchins. *Environmental Science & Technology*, 51(7): 3640–3648, mar 2017. doi: 10.1021/acs.est.6b05138. URL <https://doi.org/10.1021/acs.est.6b05138>.
- 531 [19] F. Ragazzola, L. C. Foster, C. J. Jones, T. B. Scott, J. Fietzke, M. R. Kilburn, and D. N. Schmidt. Impact of high CO<sub>2</sub> on the geochemistry of the coralline algae lithothamnion glaciale. *Scientific Reports*, 6(1), feb 2016. doi: 10.1038/srep20572. URL <https://doi.org/10.1038/srep20572>.
- 532 [20] Aldo Abarca. *Estudio mecánico estructural sobre valvas de ostiones (Argopecten Purpuratus) sometidas a escenarios de cambios climáticos*. PhD thesis, 2018. URL [http://repositorio.usach.cl/R/FHS2AQ8HEXA7HA3F2X4I19IE7UG7RA365HGUYLQPVRMSYYAB5L-01751?func=results-jump-full&set\\_entry=000004&set\\_number=000165&base=GEN01](http://repositorio.usach.cl/R/FHS2AQ8HEXA7HA3F2X4I19IE7UG7RA365HGUYLQPVRMSYYAB5L-01751?func=results-jump-full&set_entry=000004&set_number=000165&base=GEN01).
- 533 [21] Malte Meinshausen, S. J. Smith, K. Calvin, J. S. Daniel, M. L. T. Kainuma, J-F. Lamarque, K. Matsumoto, S. A. Montzka, S. C. B. Raper, K. Riahi, A. Thomson, G. J. M. Velders, and D.P. P. van Vuuren. The RCP greenhouse gas concentrations and their extensions from 1765 to 2300. *Climatic Change*, 109(1-2):213–241, August 2011. doi: 10.1007/s10584-011-0156-z. URL <https://doi.org/10.1007/s10584-011-0156-z>.
- 534 [22] ASTM Int. Designation: E8/E8M – 16a Standard Test Methods for Tension Testing of Metallic Materials. *ASTM INTERNATIONAL*, pages 1–27, 2016. doi: 10.1520/E0008\_E0008M-16A.
- 535 [23] Robert R. Sokal and F Rohlf. Biometry : the principles and practice of statistics in biological research / robert r. sokal and f. james rohlf. *SERBIULA (sistema Librum 2.0)*, 04 2013.
- 536 [24] J.Lawrence Katz and Alain Meunier. The elastic anisotropy of bone. *Journal of Biomechanics*, 20 (11-12):1063–1070, jan 1987. doi: 10.1016/0021-9290(87)90024-8. URL [https://doi.org/10.1016/0021-9290\(87\)90024-8](https://doi.org/10.1016/0021-9290(87)90024-8).
- 537 [25] Juan Velázquez, Carlos Arregui, and Gabriel Buggeda. *Modelo constitutivo para tejido óseo humano: Propiedades mecánicas del hueso cortical de costilla*. PhD thesis, Universitat Politècnica de Catalunya, 2015.
- 538 [26] Peter J. Blau and Joseph R. Davis. *ASM handbook. nonferrous alloys and special-purpose materials*. ASM International, 2000.
- 539 [27] MT Huber. Die theorie des kreuzweise bewehrten eisenbetonplatten. *Der Bauingenieur*, 4:354–392, 1923.
- 540 [28] Vladimír Panc. *Theories of elastic plates*, volume 2. Springer Science & Business Media, 1975.
- 541 [29] R. B. Rusu and S. Cousins. 3d is here: Point cloud library (pcl). In *2011 IEEE International Conference on Robotics and Automation*, pages 1–4, 2011.
- 542 [30] Xiaowu Li, Zhinan Wu, Feng Pan, Juan Liang, Jiafeng Zhang, and Linke Hou. A geometric strategy algorithm for orthogonal projection onto a parametric surface. *Journal of Computer Science and Technology*, 34(6):1279–1293, November 2019. doi: 10.1007/s11390-019-1967-z. URL <https://doi.org/10.1007/s11390-019-1967-z>.
- 543 [31] Daniel Cañas, Claudio M. García-Herrera, Emilio A. Herrera, Diego J. Celentano, and Bernardo J. Krause. Mechanical characterization of arteries affected by fetal growth restriction in guinea pigs (*Cavia porcellus*). *Journal of the Mechanical Behavior of Biomedical Materials*, 88:92–101, 2018. ISSN 18780180. doi: 10.1016/j.jmbbm.2018.08.010. URL <https://doi.org/10.1016/j.jmbbm.2018.08.010>.
- 544 [32] Jonathan Y.S. Leung, Bayden D. Russell, and Sean D. Connell. Mineralogical Plasticity Acts as a Compensatory Mechanism to the Impacts of Ocean Acidification. *Environmental Science and Technology*,

- 578 51(5):2652–2659, 2017. ISSN 15205851. doi: 10.1021/acs.est.6b04709.
- 579 [33] Luca Telesca, Lloyd S. Peck, Trystan Sanders, Jakob Thyrring, Mikael K. Sejr, and Elizabeth M.  
580 Harper. Biomineralization plasticity and environmental heterogeneity predict geographical resilience  
581 patterns of foundation species to future change. *Global Change Biology*, 25(12):4179–4193, 2019. ISSN  
582 13652486. doi: 10.1111/gcb.14758.
- 583 [34] Antonio G. Checa, Elena Macías-Sánchez, Elizabeth M. Harper, and Julyan H.E. Cartwright. Organic  
584 membranes determine the pattern of the columnar prismatic layer of mollusc shells. *Proceedings of the  
585 Royal Society B: Biological Sciences*, 283(1830), 2016. ISSN 14712954. doi: 10.1098/rspb.2016.0032.

586    **List of Figures**

587    1	Specification for grips and samples for the tensile tests. Figure 1a shows the sample design for the tensile test, the principals directions and orientations of the samples. Figure 1b shows the cross sectional area of the samples and how its estimated. Figure 1c shows the tensile test assembly. All dimensions shown in mm. . . . .	6
592    2	Flexocompression test configuration, showing the base for flexocompression test and the configuration of the test, in which the punch is located in the <i>umbo</i> of the shell (outer surface). . . . .	7
595    3	Parametric surfaces adjusted to the barycentres of meshes for 45° tensile and full shell specimens. . . . .	9
597    4	Element directions fitting for meshes used in FEM simulations. In the boxes is shown the orientations of the particular coordinated system in relation to an global orthotropic behavior. . . . .	10
600    5	Flowchart of the fitting procedure of elastic properties through numerical simulations. . . . .	11
602    6	Results of the tensile test apparent behavior in engineering stress ( $\sigma$ ) against engineering strain ( $\epsilon$ ). Figures 6d, 6f, 6e show a comparison of the mechanical behavior on the maximum strain, maximum engineering stress, and the elastic modulus. (●): extreme values of the distribution. . . . .	14
606    7	Figure 7a show the behavior of complete shells in flexocompression test. It is shown at the application of force on the shell and displacement of the punch (vertical) in the umbo. Figure 7b show the comparison of the behavior of shells subjected to flexocompression tests. The top graph shows the maximum force applied to the shell [N] and the bottom graph shows the displacement of the punch [mm] before the fracture. (●): extreme values of the distribution. . . . .	15
612    8	Results of simulations and comparison with experimental tests. Figure 8a shows the simulation results of the tensile test, both for the elastic properties fitting stage (longitudinal and transversal direction) and for the validation stage (diagonal). Figure 8b shows the validation of the orthotropic model adopted with the adjusted properties obtaining an error of approximately 23%. . . . .	17
617    9	Principal stresses magnitude and directions (in the boxes) in the shell-punch contact area. . . . .	19

619 **List of Tables**

620      1	Maximum values for the behaviour of shells in the flexocompression test. 621      Mean and standard error of force and displacement. . . . .	16
622      2	The table shows the results of the unfitted experimental elastic properties and 623      the fitted elastic properties obtained from the tensile test and their respective 624      fit. . . . .	17
625      3	The table shows the results in comparison to the properties reported by 626      Abarca [20] of uniaxial compression tests in the three orthogonal directions 627      in comparison to those obtained from the tensile test, both experimental and 628      its fitting as well as the difference obtained between both calculated as per- 629      centage relative error. . . . .	17
630      4	Alignment between principal stresses directions ( $\sigma_I$ , $\sigma_{II}$ y $\sigma_{III}$ ) and orthotropic 631      directions (Longitudinal, Transversal and Thickness) in the shell-punch con- 632      tact area produced by the effects of compressive stresses (outer surface) and 633      tensile stresses (inner surface), as shown in Figure 9. . . . .	18